ADVANCED FUNCTIONAL MATERIALS
www.afm-journal.de

Gradient Interlayer Promotes Highly Stable Zn Metal Anodes for High-Performance Zn-Ion Batteries

Zhenjing Jiang, Siwei Fan, Zijuan Du, Wei Zhang, Ruwei Chen, Hang Yang, Jie Chen, Zhe Cui, Fuhan Cui, Guoju Zhang, Chongyang Zhu, Shuangying Lei, Guanjie He, Kuibo Yin,* and Litao Sun**

Zn metal anodes hold great promise for aqueous batteries due to its high theoretical capacity, suitable redox potential, good compatibility with water-based electrolytes, and facile accessibility. However, its practical application remains a severe challenge, as Zn dendrite growth and parasitic reactions (e.g., hydrogen evolution reaction (HER), corrosion, and passivation) incur poor cyclic stability. Herein, a unique multi-filtration-concentration gradient interlayer integrating a three-dimensional (3D) structure is constructed to protect the Zn metal anode. Thanks to the rationally engineered interface, this gradient interlayer can filtrate the water molecules in the electrolyte to inhibit HER. Meanwhile, the zincophilic alloy concentrates Zn^{2+} ions and homogenizes electric field distribution to ensure uniform Zn deposition. Consequently, with its protection, the symmetric Zn||Zn cell maintains stable cycles for 3330 h with a low overpotential of 14.1 mV. It also endows superior cycle stability of the full-cells that coupled the Zn anode with MnO_2 and $NH_4V_4O_{10}$ cathodes under a low N/P ratio, including the Zn||iodine pouch cells. This works provides a facile and industrially applicable method on effectively improving Zn metal anodes for aqueous batteries.

1. Introduction

To tackle the global warming and energy crisis, the development of grid-scale energy storage devices based on safe, low-cost, and eco-friendly electrochemical technologies becomes urgent.[1–3] In this regard, aqueous rechargeable metal-ion battery technologies including lithium-ion batteries, sodium-ion batteries, and magnesium-ion batteries, etc., provide a feasible way for the green energy storage.[4–6] Among them, aqueous zinc-ion batteries (AZIBs) featuring high safety and cost-effectiveness are considered as a promising energy storage technology. The high theoretical capacity (5855 mAh cm^{-3}) and relatively low redox potential (–0.76 V vs. standard hydrogen electrode (SHE)) of the Zn metal anode enable a considerable energy density of the batteries.[7] However, the Zn metal anode suffers from severe challenges from the rampant water-induced parasitic reactions (corrosion, hydrogen evolution reaction (HER), and byproduct accumulation) and Zn dendrite growth.[8] The continuous consumption of electrolyte/electrode and the Zn dendrites growth during cycling result in a low Coulombic efficiency (CE), uncontrollable interfacial properties, and short lifespan of the Zn metal-based batteries.[9]

Recently, numerous strategies based on interfacial modification have been proposed to protect the Zn metal anode by regulating electric field distribution and introducing zincophilic sites.[10–14] For example, the designed zincophilic Sb/Sb_2Zn_3 and Te/ZnTe interlayers are known to homogenize the distribution of electric field and reduce the barrier for Zn nucleation, thereby ensuring a fast and uniform Zn nucleation behavior.[12,15] Whereas, although the Zn dendrite is effectively prevented through the above strategies, the parasitic reactions on the Zn anode remain inevitable as the Zn metal tend to electrodeposit on the top of the conductive interlayer (near the separator).[16] On the other hand, the water-induced HER and corrosion reaction will also happen at the interface between newly deposited Zn metal and the electrolyte. It is worth noting that the hydrophobic interface can remove the parasitic reactions at the Zn anode/electrolyte interface. For example, the hydrophobic Tween-20 and zinc

Z. Jiang, F. Cui, G. Zhang, C. Zhu, S. Lei, K. Yin, L. Sun
SEU-FEI Nano-Pico Center, Key Laboratory of MEMS of Ministry of Education
Southeast University
Nanjing 210096, P. R. China
E-mail: yinkuibo@seu.edu.cn; slt@seu.edu.cn

Z. Jiang, Z. Du, W. Zhang, R. Chen, H. Yang, J. Chen, Z. Cui, G. He
Christopher Ingold Laboratory, Department of Chemistry
University College London
London WC1H 0AJ, UK
E-mail: g.he@ucl.ac.uk

S. Fan
School of Environmental and Chemical Engineering
Shanghai University
Shanghai 200444, P. R. China

Z. Du
State Key Laboratory of Silicate Materials for Architectures
Wuhan University of Technology
Wuhan 430070, P. R. China

The ORCID identification number(s) for the author(s) of this article can be found under https://doi.org/10.1002/adfm.202524105

DOI: 10.1002/adfm.202524105

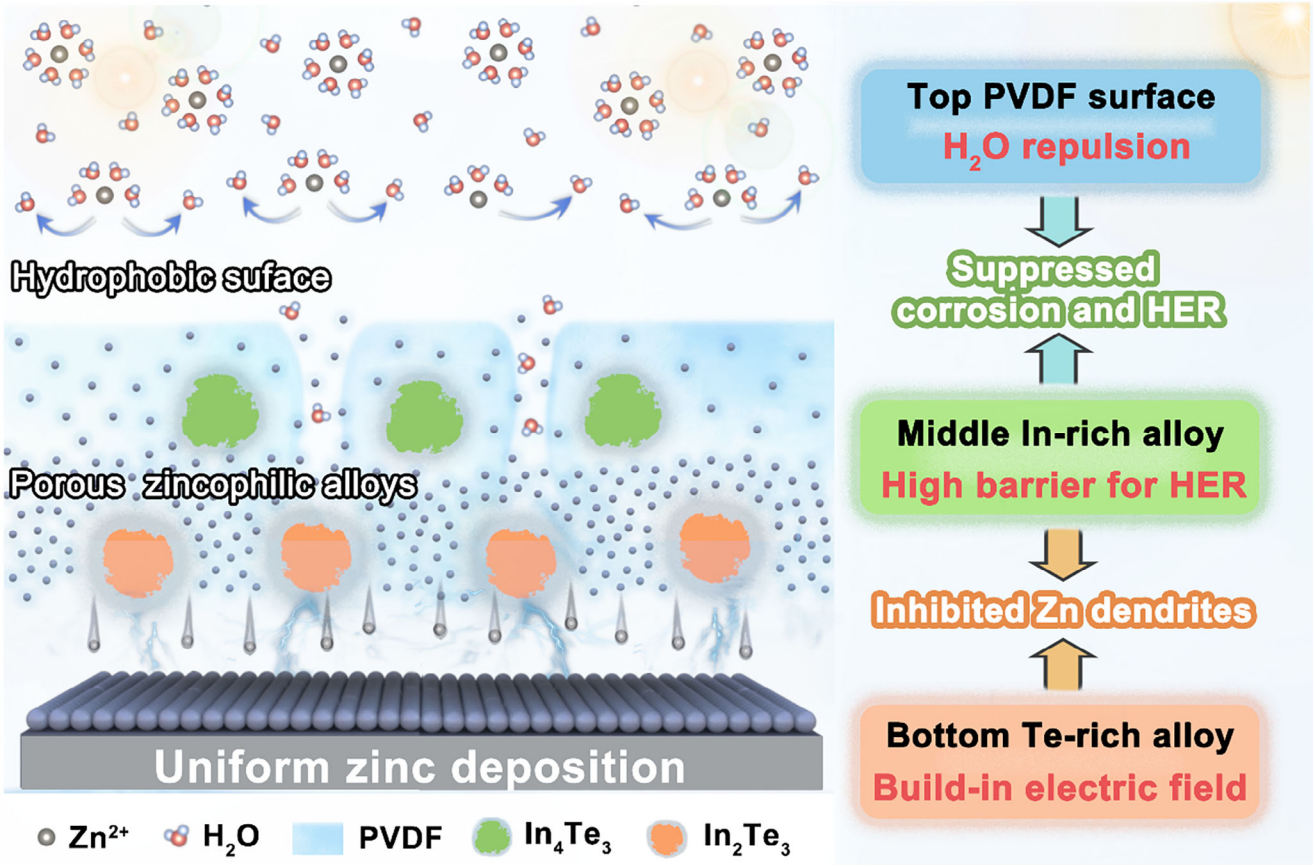

Scheme 1. Illustrate multiple functions of the designed gradient interlayer. The constructed gradient interlayer with 3D structures that consists of PVDF, In_4Te_3 alloy, and In_2Te_3 alloy realizes the step-by-step water elimination/zinc-ion concentration behavior.

perfluorovalerate interlayers significantly reduce the HER overpotential and the corrosion current on Zn anodes, thereby effectively improving its reversibility and lifespan.[17,18] Regrettably, those insulating interface generally grants Zn metal anodes the sluggish Zn^{2+} ion transport kinetics, therefore hindering their application in high-power energy storage devices.

To solve above dilemmas, multilayers (e.g., CA/SA, MXene/Ag, and PAH/PAA)[19–21] and three-dimensional (3D, e.g., $CuZn_5$, ZnO, and graphene arrays)[22–24] artificial interlayers are designed to enable the uniform and fast Zn^{2+} ion deposition, while protect the Zn anode after initial nucleation. However, the spontaneous assembly process of those multilayer artificial interlayers is greatly influenced by the preparation conditions, which may leads to uneven thickness of the interfacial layer and further cause the formation of Zn dendrites. The high density of CuZn alloys (8.5–8.9 g cm^{-3}) and poor chemical/physical stability of the ZnO and graphene would impair the energy density and interfacial stability of the battery.[22,25,26] Besides, the Sand's equation reveals that the metal deposition process is mainly affect by the initial metal-ion concentration, local current density, and ionic mobility.[27] Accordingly, many efforts have made to avoid the formation of Zn dendrite. Such as the 3D structure is constructed to reduce the local current density and the formation of ohmic contact can enhance the ionic mobility, which also enhanced the Zn deposition kinetics.[28–30] That is, both the structure and preparation method of interlayer, as well as the mechanical/chemical properties of the interlayer materials should be comprehensively considered to realize the practical application of AZIBs.

The special gradient structures allow the integration of multiple materials with different properties in an interlayer, thereby ensuring comprehensive protection for the Zn metal anode. Here, we design a gradient interlayer noted as Grad@Zn (from top to bottom are polyvinylidene difluoride (PVDF), In_4Te_3 alloy, and In_2Te_3 alloy, respectively) with a porous structure on the Zn anode through a facile spray method (Figure S1, Supporting Information). The step-by-step filtration-concentration effect of this gradient interlayer, illustrated in **Scheme 1**, is determined by combining focused ion beam-scanning electron microscope (FIB-SEM), finite element simulation, and density functional theory (DFT) calculation. Specifically, the top hydrophobic PVDF layer repels the water molecules from the Zn metal to avoid its corrosion in the electrolyte, and the middle In-rich-alloy layer shows a high dissociation energy barrier for HER. Those zincophilic alloys not only can concentrate Zn^{2+} ions in the channels of the interlayer, but also induce the uniform electric field and ion flux toward themselves (ascribed to the electrical conductivity difference compared to PVDF) to homogenize Zn deposition. Moreover, the built-in electric field forms under the bottom Te-rich-alloy layer can accelerate Zn^{2+} ions deposition, and the small shear modulus of InTe alloys (Figure S2a,

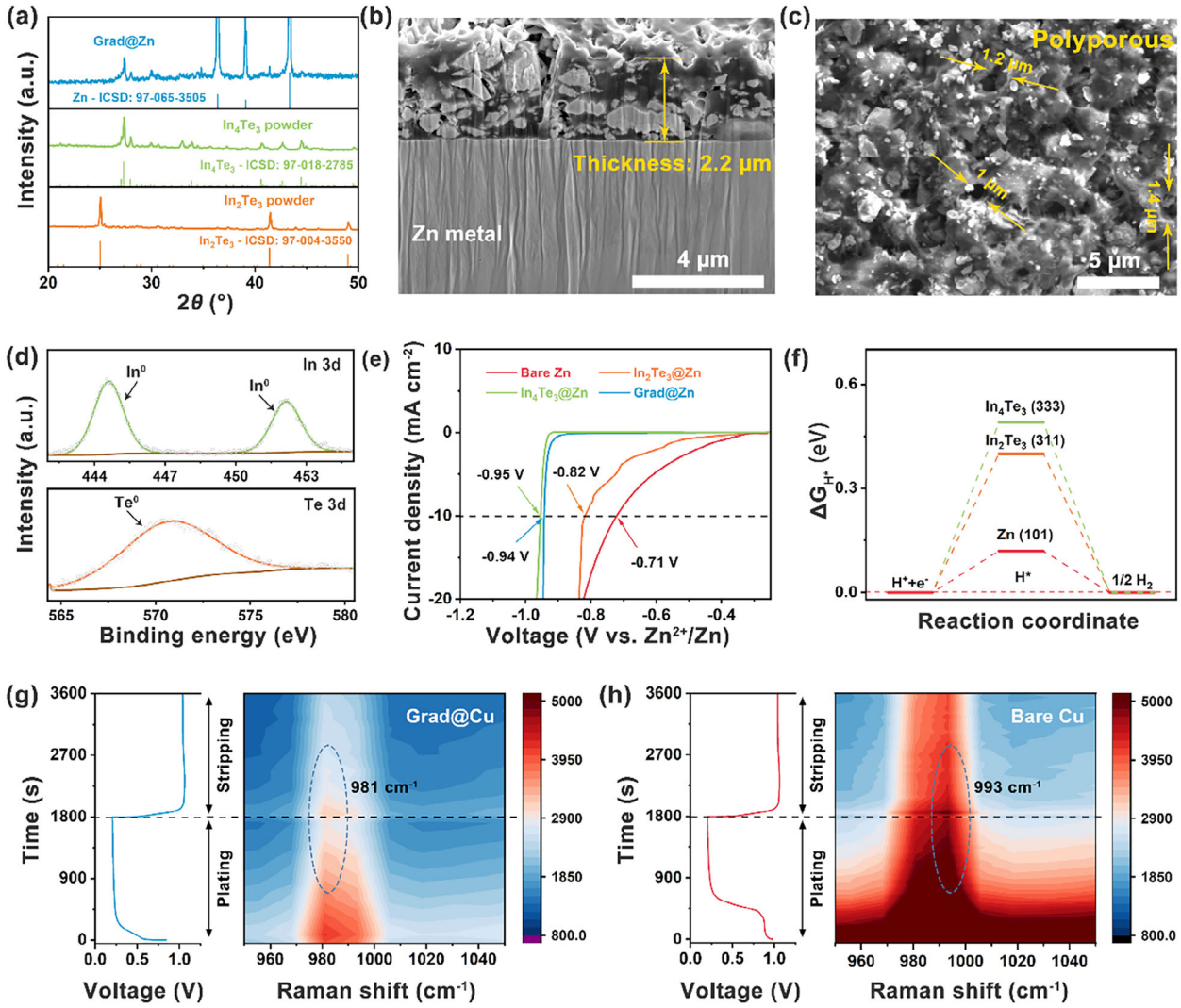

Figure 1. Structural characterization and HER detection of the electrodes with gradient interlayer. a) XRD patterns of Grad@Zn anode, In_2Te_3 alloy and In_4Te_3 alloy. b) Cross-section SEM image of Grad@Zn anode. c) The top view SEM image of Grad@Zn anode. d) In 3d and Te 3d high resolution XPS spectra of the gradient interlayer. e) Linear sweep voltammetry (LSV) curves of the bare Zn, In_2Te_3@Zn, and Grad@Zn anodes. f) Calculated free-energy diagram on the In_4Te_3 (311), In_2Te_3 (333), and Zn (101) facets for the HER. The in-situ Raman spectra of g) Grad@Cu and h) bare Cu electrodes during the Zn plating/stripping process with corresponding charge/discharge curves.

Supporting Information) also realize the excellent interlayer compatibility during cycling. Consequently, the lifespan of symmetry cell with Grad@Zn anode prolongs to 594 h even at a large current density of 10 mAh cm^{-2}. Moreover, under limited Zn excess, the discharge capacity of the Grad@Zn||MnO_2 cell retained 93.3% after 140 cycles at a current density of 0.2 A g^{-1}, is superior to most of the reported Zn anode modification strategies up to data. Those findings show that the 3D gradient interlayer holds great potential for practical applications in AZIBs.

2. Results and Discussion

2.1. Structure and Performance of the Gradient Interlayer

It is well known that the In metal possesses a high redox potential (In^{3+}/In, –0.342 V vs SHE), thus can effectively delay the onset potential for HER on the Zn metal anode.[15] Meanwhile, the Te cluster (Te^{2+}/Te, –0.510 V vs SHE) is reported to work as a zincophilic host to guide the uniform Zn deposition.[31] Therefore, based on In_2Te_3 alloy, In_4Te_3 alloy, and PVDF, we constructed a uniform gradient interlayer on the Zn metal anode as confirmed by the wide-view SEM image (Figure S3, Supporting Information). It is seen that the electron beam irradiation caused the depression of PVDF layer on the anode surface. As shown in **Figure 1a**, the X-ray diffraction (XRD) patterns of prepared powder samples correspond to the Bragg peaks of In_4Te_3 (ICSD: 97-018-2785) and In_2Te_3 (ICSD: 97-004-3550). This indicates that the pure In_4Te_3 and In_2Te_3 alloys were successfully prepared via double spraying methods. Besides, all the Bragg peaks of the two alloys and Zn metal (ICSD: 97-065-3505) can be observed from the XRD pattern of the Grad@Zn anode, implying the gradient interlayer was constructed. The corresponding cross-section

SEM image of FIB-milled Grad@Zn is acquired as depicted in Figure 1b. It is found that the constructed interlayer was tightly fitted to the Zn anode with a thickness of about 2.2 μm. Moreover, the PVDF layer covered the surface of the interlayer and significantly deformed after the electron beam irradiating and ion beam milling. In addition, lots of pores are observed to uniformly form in the artificial interlayer due to the violent solvent evaporation during the spray process. This is confirmed by the cross-section and top-view SEM images (Figure 1c). The unique polyporous morphology constitutes the 3D framework of interlayer and improves the wettability of the electrolyte (Figure S2b, Supporting Information).[32]

In addition, as verified by the high-resolution In 3d and Te 3d XPS spectra in Figure 1d, only the In^0 and Te^0 existed in the gradient interlayer, implying the pure InTe alloys powders are highly stable during the preparation process. Furthermore, the Zn metal anodes modified with single In_2Te_3 or In_4Te_3 alloy interlayer were prepared through the same process and noted as In_2Te_3@Zn and In_4Te_3@Zn, respectively. The linear sweep voltammetry (LSV) measurement of bare Zn, In_2Te_3@Zn, In_4Te_3@Zn, and Grad@Zn anodes was conducted to evaluate the ability of constructed interlayers in inhibiting HER on Zn anode. As shown in Figure 1e, compared to bare Zn anode (–0.71 V), the on-set potential of HER negatively shifts on the In_2Te_3@Zn (–0.82 V), In_4Te_3@Zn (–0.95 eV) and Grad@Zn anodes (–0.94 V), respectively. Meanwhile, the calculated corrosion current decreases from 15 μA cm^{-2} to 5, 1.2 and 1.5 μA cm^{-2} on those Zn anodes (Figure S4, Supporting Information). All the above verify the excellent performances of the InTe alloy interlayers, especially the In-rich alloy layer, in inhibiting the water-induced side reactions. To clarify the reason for the suppressed HER on the Zn metal anode, the Gibbs free energies of the H atom on In_4Te_3 (333), In_2Te_3 (311), and Zn (101) facets were compared through the DFT calculation. The H atom adsorbed models are built based on the XRD pattern of the prepared InTe alloys (Figure S5, Supporting Information). Apparently, the Zn metal shows a small free energy for H atom adsorption (0.12 eV, Figure 1f), indicating the much inclined to happen the HER. By contrast, the In_4Te_3 alloy delivers the highest free energy of 0.51 eV compared to Zn metal and In_2Te_3 alloy (0.40 eV), implying the high difficulty occurrence of HER on its surface, which is also consistent with the LSV result.

The in-situ Raman measurement was applied to investigate the accumulation of byproducts on the Cu electrode surface during Zn plating/stripping cycles. The Cu electrode with gradient interlayer (denoted Grad@Cu) was prepared through the same method as Grad@Zn. The unmodified Cu was noted as bare Cu. As displayed in Figure 1g,h, the bands in the range of 970-1005 cm^{-1} belong to the SO_4^{2-} species in the electrolyte and the formed $Zn_4SO_4(OH)_6{\cdot}xH_2O$ (ZHS) on the Cu electrode. On the Grad@Cu electrode, this band is significantly weakened and shifts to 981 cm^{-1} during the Zn plating process. The band at 981 cm^{-1} is ascribed to the "free" ν-SO_4^{2-} in the electrolyte, indicating that the HER and accompanied byproducts are effectively inhibited with the protection of this gradient interlayer. In contrast, because of the large amounts of byproducts induced by the severe HER, a much stronger band can be observed on the bare Cu electrode and transfers to 993 cm^{-1} during the continuous Zn plating process.[33] In a word, a gradient and polyporous interlayer was successfully constructed on the Zn anode, which can suppress the HER as well as the byproducts accumulation effectively.

2.2. Reversibility and Stability of the Zn Metal Anodes

The reversibility and stability of the Zn plating/stripping behavior were tested to determine the validity of this gradient interlayer. As shown in **Figure 2**a, at a current density of 1 mA cm^{-2}, the Zn||Cu half-cell with Grad@Cu electrode exhibits the highest average CE (ACE) of 99.2% and sustains stable cycles for more than 720 times. The In_4Te_3@Cu electrode also delivers a high ACE of 98.9%, but drastically fluctuates and fails after 365 cycles. In sharp contrast, the In_2Te_3@Cu can only cycle for 191 times with a relatively low ACE of 98.1%, while the ACE of bare Cu electrode is only 95.7% which fails after 90 cycles. Besides, the Zn||Cu cell with Grad@Cu electrodes also shows the lowest polarization voltage (40.6 mV at 80th cycle, Figure 2b) compared to the cells with In_2Te_3@Cu (49.4 mV), In_4Te_3@Cu (59.6 mV) and bare Cu (89.8 mV), respectively. When the current density increases to 5 mA cm^{-2}, the excellent properties of the Grad@Cu electrode become apparent as it can cycle for 600 times with a high ACE of 99.5%, and the In_4Te_3@Cu can also cycle for 378 times with an ACE of 99.3% (Figure 2c). Unfortunately, the In_2Te_3@Cu and bare Cu electrodes deliver much lower ACEs of 98.9% (for 223 cycles) and 98.5% (for 141 cycles), respectively.

The long-term cyclic stability of Zn||Zn symmetric cells with bare Zn, In_2Te_3@Zn, In_4Te_3@Zn, and Grad@Zn anodes was also tested. Apparently, at a current density of 1 mA cm^{-2}, the cells with Grad@Zn and In_2Te_3@Zn anodes show a small overpotential during cycling. However, the overpotential of In_4Te_3@Zn anode is larger than that of bare Zn (Figure 2d). In addition, the symmetric cell with Grad@Zn anode achieves a cyclic lifespan of 3330 h, which is longer than 995, 1100, and 113 h for In_2Te_3@Zn, In_4Te_3@Zn, and bare Zn anodes, respectively. The sudden increased overpotential of cell with In_2Te_3@Zn anode before short-circuiting is ascribed to the depletion of electrolyte, which also emphasizes the strong ability of In_4Te_3 layer to suppress side reactions. Furthermore, the symmetric cells were tested at the current densities of 2, 5, 10, and 20 mA cm^{-2} with a fixed areal capacity of 1 mAh cm^{-2}. As shown in Figure 2e, the cells with Grad@Zn and In_2Te_3@Zn anodes exhibit significantly lower overpotentials compared to In_4Te_3@Zn and bare Zn anodes, implying the faster Zn deposition kinetics. In addition, the cells were tested at a high current density of 10 mA cm^{-2} with a high capacity of 10 mAh cm^{-2} (the Zn utilization rate reached 33.6%). Surprisingly, the symmetric cell with Grad@Zn anode sustains stable cycle for about 594 h (Figure 2f), is much superior to the cells with In_2Te_3@Zn (199 h), In_4Te_3@Zn (254 h), and bare Zn (54 h) anodes. The prolonged cyclic lifespans of Grad@Zn and In_4Te_3@Zn anodes compared to In_2Te_3@Zn further emphasis the crucial role of the suppression of HER in stabilizing Zn anodes.[34] In short, our designed gradient interlayer grants Zn metal anode the ultralong lifespan even at a large area capacity of 10 mAh cm^{-2}, which is superior to all the recently reported Zn anodes based on surface modification strategies (Figure 2g; Table S1, Supporting Information).

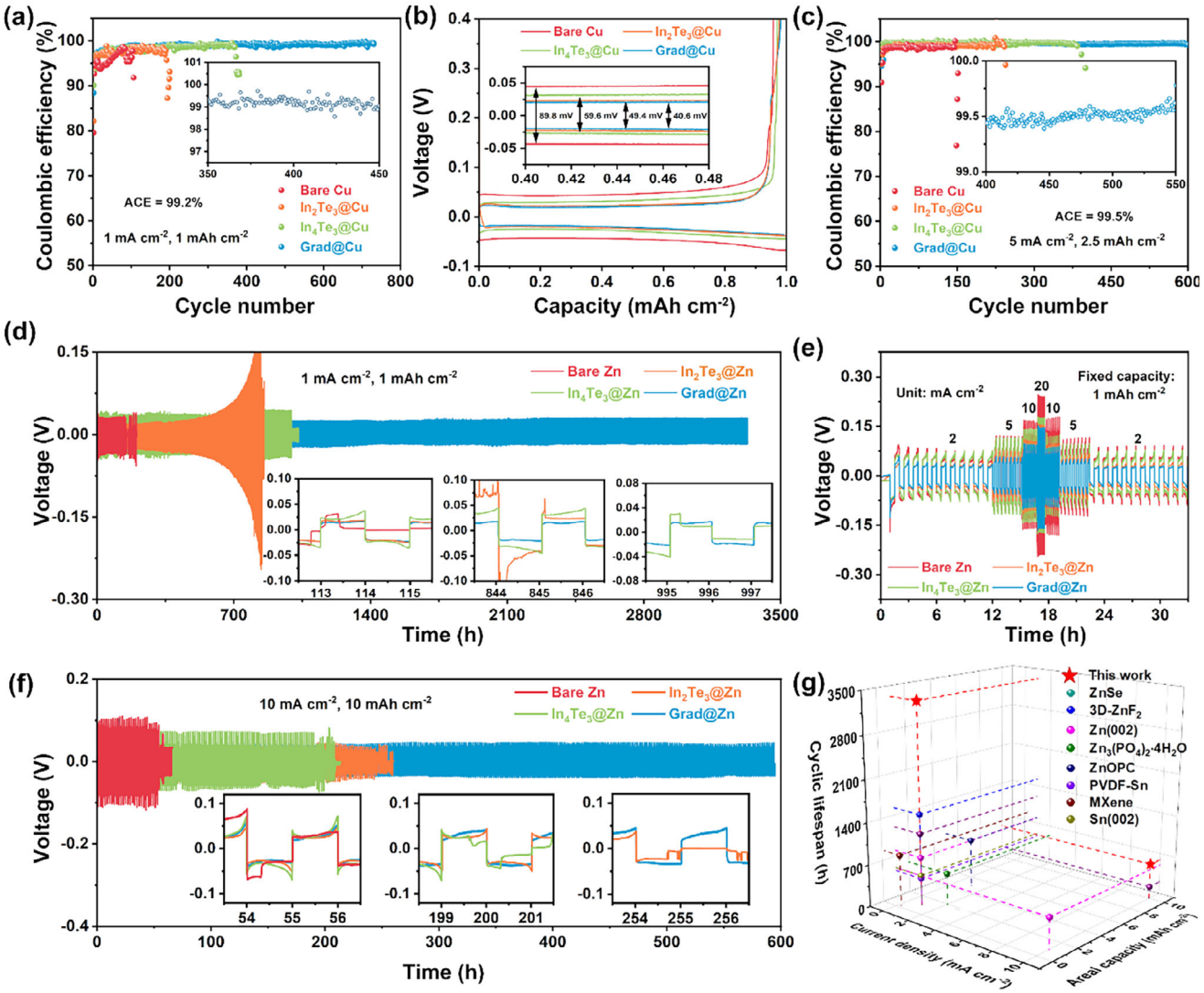

Figure 2. Electrochemical performance of the half-cells and symmetric cells. a) CEs of Zn||Cu half-cells at 1 mA cm^{-2}/1 mAh cm^{-2} and b) the corresponding charge/discharge curves of cells at 80th cycle. c) CEs of Zn||Cu half-cells with different anodes at 5 mA cm^{-2}/2.5 mAh cm^{-2}. d) The electrochemical performance of Zn||Zn symmetry cells at 1 mA cm^{-2}/1 mAh cm^{-2}. e) Rate performance of Zn||Zn symmetry cells with a fixed capacity of 1 mAh cm^{-2}. f) The electrochemical performances of Zn||Zn symmetry cells at 10 mA cm^{-2}/10 mAh cm^{-2}. g) Lifespan comparison of this work with recently reported modified Zn anodes.

2.3. Characterization of the Interfacial Performance

To clarify the origin of the excellent interfacial performance of the Grad@Zn anode, e.g., fast Zn^{2+} ion transport and deposition kinetics, the DFT calculation was conducted. Because of the considerable work function difference between Zn metal (3.95 eV) and In_2Te_3 alloy (5.51 eV, Figure S6a,b, Supporting Information), an ohmic contact interface is formed between them.[35] As confirmed in **Figure** 3a, the nearly straight I–V curve and the symmetrical logarithmic result represent the formation of an ohmic contact. Consequently, amounts of negative electrons will accumulate at the anode interface to generate a build-in electric filed. This electric field shows a strong electrostatic attraction to the Zn^{2+} ions in the electrolyte, thereby accelerating their transport towards the Zn anode (Figure 3b).[36] However, the work function of the In_4Te_3 alloy is merely 4.45 eV, thus no ohmic contact forming between the alloy and the Zn metal (Figure S6c–e, Supporting Information). Therefore, compared to the R-Grad@Zn and bare Zn anodes, the Grad@Zn anode exhibits a much higher Zn^{2+} ion transfer number and a lower charge transfer resistance (before cycles) of the symmetric cell (Figure 3c; Figure S7, Supporting Information). In addition, the charge transfer resistances of the cell with the Grad@Zn anode normally unchanged after 5, 10, 20, and 40 cycles, while the resistance of bare Zn anode increases about one-fold (Figure 3d; Figure S8, Supporting Information).

Furthermore, as displayed in Figure 3e, the charge difference pictures of different models show the interaction between Zn atom and In_2Te_3 (333) facet is the strongest, thus delivering a high binding energy of 0.63 eV (Figure 3f). The calculated binding energies between the Zn atom and Zn (101) and In_4Te_3

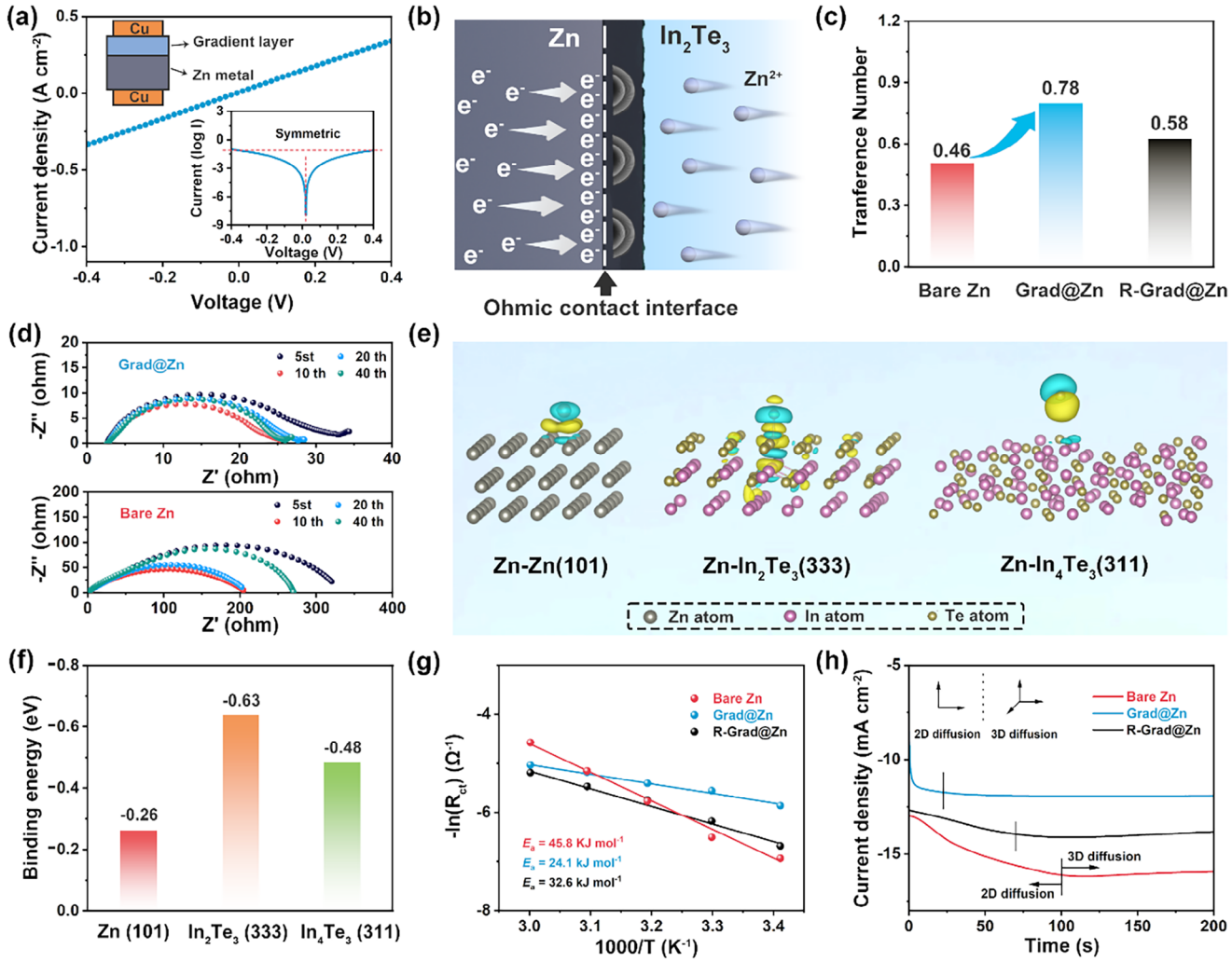

Figure 3. The Zn^{2+} ion diffusion and deposition behaviour on the Zn anodes. a) I–V curve of the Grad@Zn anode, insert: the corresponding logarithmic plots and test configuration. b) Schematic illustration of the formed ohmic contact interlayer between Zn metal and In_2Te_3 layer. c) Calculated Zn^{2+} ion transference number on the Zn anodes. d) Nyquist spots of symmetric cells with different anodes after various cycle numbers. e) The Zn atom adsorbed models of Zn (101), In_2Te_3 (333), and In_4Te_3 (311) facets with corresponding charge difference pictures. f) Calculated binding energies of different matrixes with Zn atom adsorbed. g) Calculated activation energies and h) measured chronoamperometry (CA) curves of different Zn anodes.

(311) facets are 0.26 and 0.48 eV, respectively, which are consistent with data in the previous literature.[15] The strong electrostatic attraction from the "channel wall" of InTe alloys combined with the built-in electric field at the anode interface can effectively facilitate the desolvation and transport of Zn^{2+} ions in the electrolyte[37] Therefore, the activation energies are reduced from 45.8 kJ mol^{-1} (bare Zn) to 32.6 kJ mol^{-1} (R-Grad@Zn), and further reduced to 24.1 kJ mol^{-1} on Grad@Zn anode, as displayed in Figure 3g and Figure S9, Supporting Information. Meanwhile, the high binding energy constricts the 2D diffusion of Zn^{2+} ions on the Zn anode surface to prevent the growth of Zn dendrite.[18] As verified by the chronoamperometry (CA) result, the Zn^{2+} ions on bare Zn anode experience a long 2D diffusion process for 105 s (Figure 3h). The diffusion time reduces to 71 s on R-Grad@Zn and 23 s on the Grad@Zn anode, respectively, implying the outstanding ability of In_2Te_3 layer and the built-in electric field in suppressing Zn dendrites. In conclusion, the designed gradient interlayer not only accelerates the Zn^{2+} ion transport at the interlayer due to the formed built-in electric field but also achieves the fast and uniform Zn plating/stripping process due to the matrix is highly zincophilic, which grants the excellent interfacial properties to the prepared Grad@Zn anode.

2.4. Comparison of Zn Deposition Morphology

The Zn deposition morphology under the guidance of the constructed 3D gradient interlayer is also investigated to understand the prolonged cyclic lifespan of the Grad@Zn anode. Specifically, different amounts of Zn metal were deposited on Grad@Zn and bare Zn anodes at the current densities of 2.5, 5, and 10 mA cm^{-2}. Apparently, the Zn metal is observed to be uniformly deposited in the holes of the 3D gradient interlayer on Grad@Zn anode after 2.5 mAh cm^{-2} of Zn metal was plated, as shown in **Figure** 4a.

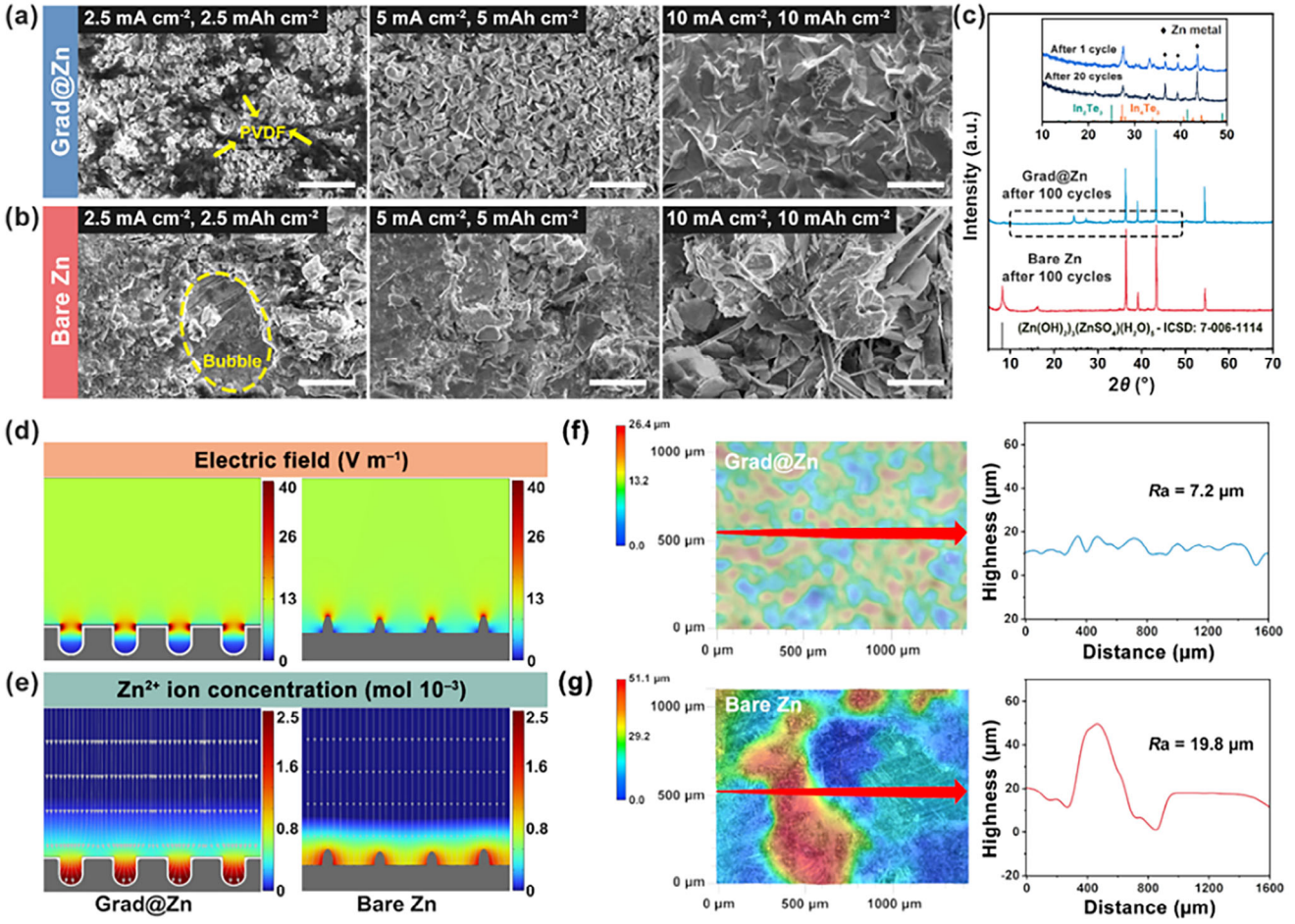

Figure 4. Characterization and simulation of the Zn deposition. SEM images of a) Grad@Zn and b) bare Zn anodes after plating 2.5, 5, and 10 mAh cm^{-2} of Zn metal, scale bar: 5 μm. c) XRD patterns of Grad@Zn and bare Zn anodes after 100 cycles, insert: XRD patterns of Grad@Zn anode after 1 and 20 cycles. Simulation of electric field distribution, Zn^{2+} ion concentration on d) bare Zn and e) Grad@Zn. Optical super depth-of-field microscope (OSM) images with corresponding surface roughness curves of f) Grad@Zn and g) bare Zn anodes after 50 cycles at 2.5 mA cm^{-2}/2.5 mAh cm^{-2}.

Combined the cross-section SEM image and corresponding EDS mapping of FIB-milled Grad@Cu electrode (Figure S10, Supporting Information), a detailed information about Zn deposition in the 3D gradient interlayer is acquired. Specifically, because of the insulating nature of the PVDF top layer, Zn metal is uniformly deposited beneath the gradient interlayer and on the walls of the channels within this interlayer, particularly around the zincophilic In_2Te_3 and In_4Te_3 alloys. When the areal capacity of deposited Zn reaches 5 mAh cm^{-2}, the deposition morphology becomes parallel to the anode surface. This is due to the stronger attraction of PVDF for Zn atoms compared to Zn metal induces a Zn^{2+}-ion-rich surface.[38] Consequently, a dense and uniform Zn deposition morphology is acquired after plating 10 mAh cm^{-2} of Zn metal. Note that the uniform Zn deposition in the channels of 3D gradient interlayer is realized even after 100 cycles with the areal capacity of 2.5 mAh cm^{-2} (Figure S11, Supporting Information), further emphasizing the long-term stability of this interlayer. By contrast, as shown in Figure 4b, the Zn metal deposition behavior on bare Zn anode is distinctly different. The heterogeneous nucleation of Zn metal is observed on bare Zn anode after the deposition of 2.5 mAh cm^{-2} of Zn metal, and the marked unnucleated area may be attributed to the emerging bubble from the HER.[39] That is, the Zn deposition process on the bare Zn anode is greatly disturbed by the parasitic reactions, which becomes further uneven after plating 5 mAh cm^{-2} of Zn metal. Ultimately, the Zn dendrites are already grown into the glass fiber membrane after plated 10 mAh cm^{-2} Zn metal, leading to the rapid short-circuit of the battery.

As a supplement, the top- and side- view SEM images of Grad@Zn and bare Zn anodes after 100 cycles with an areal capacity of 5 mAh cm^{-2} were detected in Figure S12, Supporting Information. Obviously, the gradient interlayer realizes the uniform Zn deposition during the continuous Zn plating/stripping cycles, while the severe Zn dendrite growth occurs on the bare Zn anode. Moreover, the corresponding XRD patterns of the cycled Zn anodes were acquired to evaluate the accumulation of byproducts on the anodes during the Zn plating/stripping cycles. As shown in Figure 4c, a large amount of $(Zn(OH)_2)_3ZnSO_4(H_2O)_5$ (ICSD: 97-006-1114) is formed on the bare Zn anode after 100 cycles due to the pH fluctuation induced by the severe HER. However, with the protection of the gradient interlayer, little byproducts are detected because the HER is effectively suppressed on the Zn anode

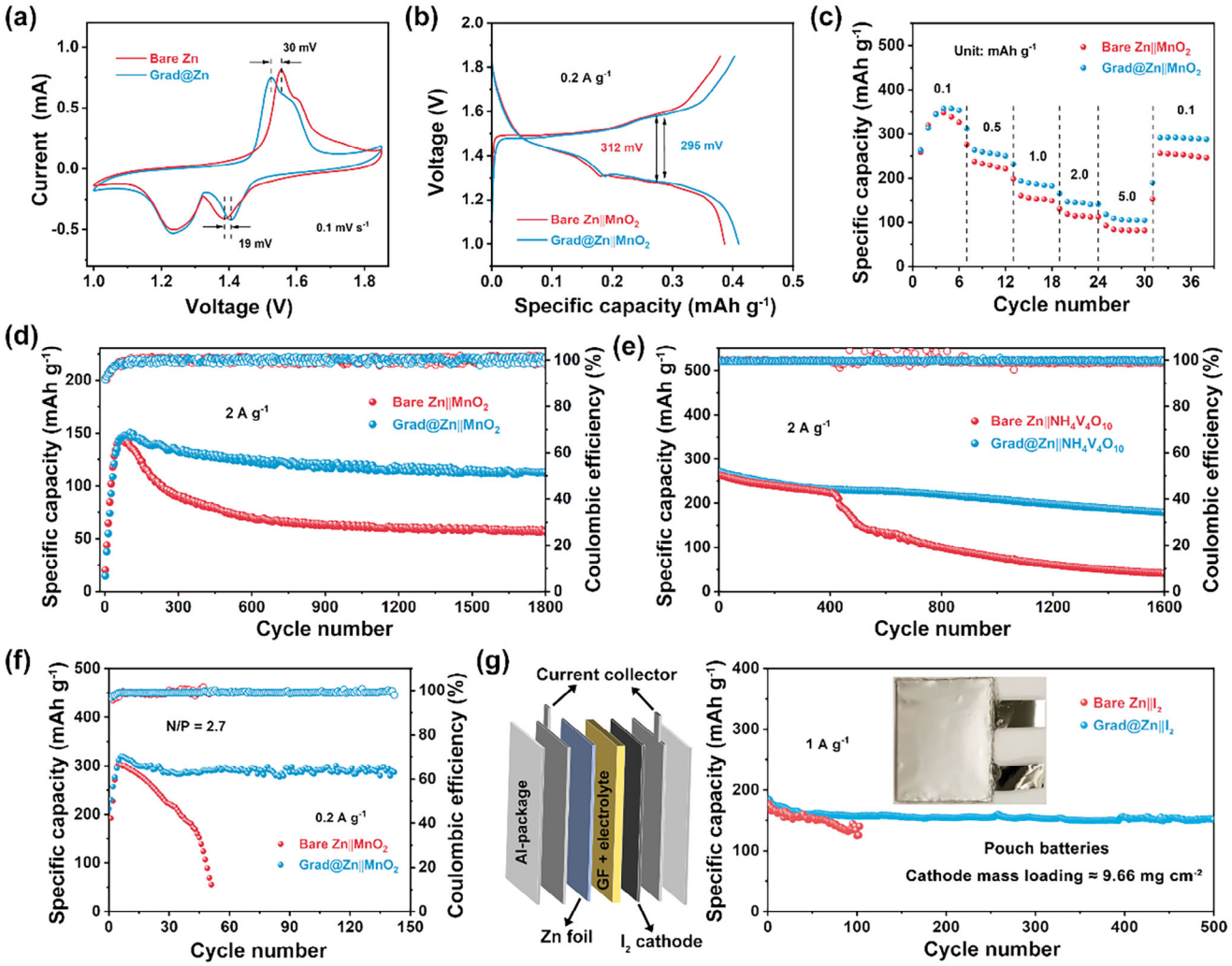

Figure 5. The electrochemical performance of the full-cells with MnO_2, $NH_4V_4O_{10}$, and I_2 cathodes. a) Cyclic voltammetry (CV) curves of Zn||MnO_2 cells at a scan rate of 0.1 mV s^{-1}. b) The charge/discharge profiles of Zn||MnO_2 cells at 0.2 A g^{-1}. c) Rate performance of Zn||MnO_2 cells with different Zn anodes. The electrochemical performance of d) Zn||MnO_2 and e) Zn||$NH_4V_4O_{10}$ cells at 2 A g^{-1}. f) The cycle performance of Zn||MnO_2 cells with different anodes (20 µm Zn anode, with a N/P ratio of 2.7) at 0.2 A g^{-1}. g) The diagram and cycle performance of Zn||I_2 pouch cells with a cathode mass loading of about 9.66 mg cm^{-2} at a current density of 1 A g^{-1}.

surface. Furthermore, the InTe alloy-based gradient interlayer is highly stable during the continuous cycles, the XRD patterns inserted in the top of Figure 4c, the diffraction peaks of alloys are preserved after 1, 20, and even 100 cycles.

To clarify the Zn deposition behavior guided by the 3D gradient interlayer, the finite element simulations of the electric field distribution and Zn^{2+} ion concentration of the Grad@Zn anode was studied, and bare Zn anode was modelled for comparison. Visibly, the insulating PVDF top layer and the conductive InTe alloys/Zn metal result in the concentrated electric field strength and Zn^{2+} ion flux toward the channel wall and the bottom of interlayer (Figure 3d,e). Therefore, the Zn metal is energetically preferred to be deposited from bottom to top in the channels of the gradient interlayer, which is also consistent with the SEM results above. In this way, the growth of Zn dendrites is effectively suppressed, realizing the significantly prolonged lifespan of the Zn metal anode. In contrast, the defects on bare Zn surface, e.g. bumps, cause the concentrated electric field strength and inhomogeneous distribution of Zn^{2+} ions around them to lead to the aggressive Zn deposition on the bumps and evolve to the dendrites.

Here, the in situ optical microscopy measurement was used to record the morphology evolution of deposited Zn on different anodes at a current density of 10 mA cm^{-2}. As exhibited in Figure S13, Supporting Information, it is observed that the Zn metal is deposited under the black gradient interlayer on the Grad@Zn anode and maintains a smooth morphology even after 15 min of Zn plating. In contrast, the Zn deposition morphology on bare Zn anode becomes uneven due to the formation and growth of Zn dendrites. Furthermore, to observe the Zn deposition behavior at the macroscale, the optical super depth-of-field microscope (OSM) images with corresponding surface roughness curves of Glass@Zn and bare Zn anodes after 50 cycles were acquired. Clearly, the Zn is deposited uniformly on the Grad@Zn anode

over a broad view range (1600 μm × 1100 μm, Figure 4f). The slight protrusion on the Grad@Zn is the area of dense interlayer channels, and the parallel growth of Zn metal along the anode surface ensures a low average surface roughness of 8.2 μm. On the contrary, due to the formation of severe Zn dendrites, the average surface roughness arrives 19.8 μm on bare Zn anode (Figure 4g). That is, the constructed gradient interlayer is durable during cycling and enables both the uniform Zn deposition and suppressed HER on the Zn anode surface simultaneously.

2.5. Electrochemical Performance of Full-Cells

The practical application potential of the designed Grad@Zn anode is evaluated by coupling with MnO_2 and $NH_4V_4O_{10}$ cathodes that prepared based on the previous literatures.[40,41] The Zn||MnO_2 cell with Grad@Zn anode deliver the similar redox/reduction peaks in the cyclic voltammetry (CV) curves compared to the bare Zn anode, indicating that the alloy interlayer does not participate in the charge/discharge reactions (**Figure 5a**). Besides, the CV curves of the full cells with Grad@Zn anode exhibit smaller polarization and higher peak intensity, implying fast electrochemical reaction kinetics.[26] As a supplement, the charge/discharge curves of Zn||MnO_2 cells in Figure 5b show the polarization voltage of Grad@Zn is reduced to 276 mV, while that of bare Zn anode is 305 mV. Consequently, the Grad@Zn||MnO_2 cell exhibits the superior rate performance at the current densities of 0.2, 0.5, 1, 2, and 5 A g^{-1}, as well as lower charge transfer resistances (Figure 5c; Figure S14, Supporting Information). When the current density returns to 0.2 A g^{-1}, 87% of the discharge capacity of the Grad@Zn||MnO_2 cell is recovered, compared to 76% for the bare Zn anode.

The self-discharge measurement is a valid method to assess the stability of Zn||MnO_2 cells. The capacity loss of the cells is mainly ascribed to the decay of the Zn metal anode.[42] Benefiting from the suppressed side reactions on the Zn anode, the discharge capacity of Grad@Zn||MnO_2 cell preserves 88.2% (1.52 V, Figure S15, Supporting Information) after resting for 72 h, the one with the bare Zn anode only remains 58.2% (1.39 V). When test at the current density of 2 A g^{-1}, the discharge capacity of Grad@Zn||MnO_2 cell exhibits a superior retention rate of 76.8% (113.2 mAh g^{-1}) after 1800 cycles, which of bare Zn||MnO_2 cell is 39.0% (56.3 mAh cm^{-2}, Figure 5d). To further evaluate the universality of the designed 3D gradient interlayer, the Grad@Zn anode was also tested in Zn||$NH_4V_4O_{10}$ cell with 2 M $Zn(CF_3SO_3)_2$ electrolyte. As displayed in Figure 5e, under the protection of the gradient interlayer, the Grad@Zn||$NH_4V_4O_{10}$ cell sustains stable cycles for more than 1600 times with a reserved discharge capacity of 170.8 mAh g^{-1}. However, although the cell with bare Zn anode also delivers a high initial discharge capacity, it quickly decays after 410 cycles accompanied by the wildly fluctuating CE, ultimately delivering a capacity of 38.41 mAh g^{-1} (38.9%) after 1600 cycles.

Furthermore, the cycle performance of the Zn||MnO_2 cells was also tested at a condition that was close to the practical application (the ratio of negative electrode capacity and positive electrode capacity decreased to 2.7). Under the current density of 0.2 A g^{-1}, both the discharge capacities of two cells with bare Zn and Grad@Zn anodes increase to 290 and 312 mAh g^{-1} after about 8 cycles for activation, as shown in Figure 5f. However, the discharge capacity of the cell with bare Zn anode rapidly fades after 46 cycles and fails after 58 cycles. Surprisingly, the cell with the Grad@Zn anode sustains a stable cycle for more than 140 times with a capacity retention rate of 93.3% (291.1 mAh g^{-1}). In addition, the assembled pouch cell with Grad@Zn anode and iodine cathode (with a high cathode mass loading of about 9.66 mg cm^{-2}) was also tested to verify the effectiveness of the constructed gradient interlayer. As displayed in Figure 5g, the discharge capacity of the pouch cell preserved 83.7% after 600 cycles at 1 A g^{-1}, implying its superior cycle stability.

3. Conclusion

In this work, we design a gradient protective interlayer with a 3D structure on the Zn metal anode and clarified its step-by-step water elimination/zinc-ion concentration behavior in stabilizing the anode. Based on DFT calculation and in situ Raman results, the HER and byproducts accumulation on the Zn anode are confirmed to be effectively suppressed by the top hydrophobic PVDF layer (repel water molecules from the anode) and middle In-rich layer (possess high Gibbs free energy for the adsorbed H atom). Besides, the generated porous zincophilic channels in gradient interlayer can concentrate Zn^{2+} ions and reduce the local current density on the anode surface, especially the bottom Te-rich alloy layer, enabling the uniform and fast Zn deposition as verified by the finite element simulations, SEM and OSM results. Furthermore, those InTe alloys possess low shear modulus and are highly stable during cycling, thereby maintaining the outstanding interfacial performance of the anode. Consequently, the gradient interlayer effectively enhances the stability and reversibility of the Zn anode. It also enables the outstanding electrochemical performance of full cells coupled with MnO_2 and $NH_4V_4O_{10}$ cathodes. The discharge capacity of Zn||I_2 pouch cell preserved 83.7% after 600 cycles with a high cathode mass loading of about 9.66 mg cm^{-2}. This work proposes a scalable strategy for integrating multiple functions into an interlayer to achieve high-performance AZIBs

Supporting Information

Supporting Information is available from the Wiley Online Library or from the author.

Acknowledgements

This work was supported by the National Natural Science Foundation of China (Nos. 12174050, and 12234005), the Natural Science Foundation of Jiangsu Province (BK20231411, and BK20222007), the Key R&D Program of Jiangsu Province (BE2021007-2), the Fundamental Research Funds for the Central Universities, the Engineering and Physical Sciences Research Council (EPSRC, EP/027433/3), and UK Research and Innovation (UKRI) under the UK government's Horizon Europe funding (101077226; EP/Y008707/1).

Conflict of Interest

The authors declare no conflict of interest.

Author Contributions

Z.J. conceived the idea, designed the experiments and analyzed the data. S.F., Z.D., W.Z., R.C., H.Y., J.C., Z.C., F.C., and G.Z. contributed to the electrochemical/materials' characterization and analysis. Z.J., C.Z., F.C., and S.L. contributed to the theoretical simulation. Z.J. and Z.D. drafted the manuscript with input from all authors. G.H., K.Y., and L.S. provided major revisions and supervised the project. All authors contributed to discussions and writing of the manuscript.

Data Availability Statement

The data that support the findings of this study are available from the corresponding author upon reasonable request.

Keywords

gradient interlayer, multi-filtration-concentration, three-dimensional structure, Zn metal anode

Received: September 10, 2025
Revised: October 19, 2025
Published online: November 12, 2025

[1] B. Obama, *Science* **2017**, *355*, 126.
[2] F. Wang, O. Borodin, T. Gao, X. L. Fan, W. Sun, F. D. Han, A. Faraone, J. A. Dura, K. Xu, C. S. Wang, *Nat. Mater.* **2018**, *17*, 543.
[3] L. S. Cao, D. Li, T. Pollard, T. Deng, B. Zhang, C. Y. Yang, L. Chen, J. Vatamanu, E. Y. Hu, M. J. Hourwitz, L. Ma, M. Ding, Q. Li, S. Hou, K. Gaskell, J. T. Fourkas, X. Q. Yang, K. Xu, O. Borodin, C. S. Wang, *Nat. Nanotechnol.* **2021**, *16*, 902.
[4] S. K. Zhan, Y. H. Zhu, Y. J. Li, X. Y. Liu, F. H. Ning, Y. H. Xie, S. G. Lu, Y. Y. Xia, J. Yi, *Adv. Funct. Mater.* **2025**, *35*, 2507573.
[5] L. Ma, M. A. Schroeder, O. Borodin, T. P. Pollard, M. S. Ding, C. S. Wang, K. Xu, *Nat. Energy* **2020**, *5*, 743.
[6] H. Y. Zhang, F. H. Ning, Y. M. Guo, S. Subhan, X. Y. Liu, S. Q. Shi, S. G. Lu, Y. Y. Xia, J. Yi, *ACS Energy Lett.* **2024**, *9*, 4761.
[7] P. J. Wang, S. Q. Liang, C. Chen, X. S. Xie, J. W. Chen, Z. H. Liu, Y. Tang, B. G. Lu, J. Zhou, *Adv. Mater.* **2022**, *34*, 2202733.
[8] W. Liu, X. Y. Liu, F. H. Ning, S. Subhan, Y. Y. Liu, Q. Li, J. J. Zhang, S. G. Lu, J. Yi, *J. Mater. Chem. A* **2024**, *12*, 11883.
[9] Q. Yang, Q. Li, Z. X. Liu, D. H. Wang, Y. Guo, X. L. Li, Y. C. Tang, H. F. Li, B. B. Dong, C. Y. Zhi, *Adv. Mater.* **2020**, *32*, 2001854.
[10] W. D. Zhang, Q. Zhao, Y. P. Hou, Z. Y. Shen, L. Fan, S. D. Zhou, Y. Y. Lu, L. A. Archer, *Sci. Adv.* **2021**, *7*, abl3752.
[11] C. Li, Z. T. Sun, T. Yang, L. H. Yu, N. Wei, Z. N. Tian, J. S. Cai, J. Z. Lv, Y. L. Shao, M. H. Rümmeli, J. Y. Sun, Z. F. Liu, *Adv. Mater.* **2020**, *32*, 2003425.
[12] X. H. Zheng, Z. C. Liu, J. F. Sun, R. H. Luo, K. Xu, M. Y. Si, J. Kang, Y. Yuan, S. Liu, T. Ahmad, T. L. Jiang, N. Chen, M. M. Wang, Y. Xu, M. Y. Chuai, Z. X. Zhu, Q. Peng, Y. H. Meng, K. Zhang, W. P. Wang, W. Chen, *Nat. Commun.* **2023**, *14*, 76.
[13] S. D. Pu, C. Gong, Y. B. Tang, Z. Y. Ning, J. L. Liu, S. M. Zhang, Y. Yuan, D. Melvin, S. X. Yang, Q. L., J. J. M. Pi, B. K. Hu, M. Jenkins, Z. X. Li, B. Y. Liu, S. C. E. Tsang, T. J. Marrow, R. C. Reed, X. W. Gao, P. G. Bruce, A. W. Robertson, *Adv. Mater.* **2022**, *34*, 2202552.
[14] J. X. Zheng, Q. Zhao, T. Tang, J. F. Yin, C. D. Quilty, G. D. Renderos, X. T. Liu, Y. Deng, L. Wang, D. C. Bock, C. Jaye, D. H. Zhang, E. S. Takeuchi, K. J. Takeuchi, A. C. Marschilok, L. A. Archer, *Science* **2019**, *366*, 645.
[15] R. Wang, S. Xin, D. L. Chao, Z. X. Liu, J. D. Wan, P. Xiong, Q. Q. Luo, K. Hua, J. N. Hao, C. F. Zhang, *Adv. Funct. Mater.* **2022**, *32*, 2207751.
[16] J. N. Hao, B. Li, X. L. Li, X. H. Zeng, S. L. Zhang, F. H. Yang, S. L. Liu, D. Li, C. Wu, Z. P. Guo, *Adv. Mater.* **2020**, *32*, 2003021.
[17] Q. Deng, S. Z. You, W. X. Min, Y. K. Xu, W. Lin, J. Lu, C. H. Yang, *Adv. Mater.* **2024**, *36*, 2312924.
[18] S. Huang, R. Tang, X. Q. Liu, Y. F. Zhang, Y. C. Tang, Z. P. Wen, M. H. Ye, Y. Yang, C. C. Li, *Energy Environ. Sci.* **2024**, *17*, 591.
[19] X. X. Cai, X. X. Wang, Z. Bie, Z. Y. Jiao, Y. R. Li, W. Yan, H. J. Fan, W. X. Song, *Adv. Mater.* **2024**, *36*, 2306734.
[20] Z. Liu, X. Y. Li, Z. H. Li, L. L. Ma, Y. Wang, C. M. Ye, M. X. Ye, J. F. Shen, *Chem. Eng. J.* **2024**, *479*, 147412.
[21] X. Y. Hu, H. B. Dong, X. Gao, Y. Dai, N. Gao, T. L. Wang, H. Z. He, X. Gao, Y. H. Dai, Y. Y. Liu, D. J. L. Brett, I. P. Parkin, G. J. He, *Nat. Commun.* **2025**, *16*, 2316.
[22] Z. J. Jiang, K. B. Yin, R. Pan, G. J. Zhang, F. H. Cui, K. L. Luo, Y. W. Xiong, L. T. Sun, *Small* **2023**, *19*, 2302995.
[23] H. J. Tian, G. X. Feng, Q. Wang, Z. Li, W. Zhang, M. Lucero, Z. X. Feng, Z. L. Wang, Y. N. Zhang, C. Zhen, M. Gu, X. N. Shan, Y. Yang, *Nat. Commun.* **2022**, *13*, 7922.
[24] T. Q. Huang, K. Xu, N. Jia, L. Yang, H. T. Liu, J. X. Zhu, Q. Y. Yan, *Adv. Mater.* **2023**, *35*, 2205206.
[25] R. T. Guo, X. Liu, F. J. Xia, Y. L. Jiang, H. Z. Zhang, M. Huang, C. J. Niu, J. S. Wu, Y. Zhao, X. P. Wang, C. H. Han, L. Q. Ma, *Adv .Mater* **2022**, *34*, 2202188.
[26] Y. B. Zhu, Y. C. Wang, B. Wu, Z. Z. He, J. Xia, H. A. Wu, *Nano Lett.* **2021**, *21*, 8401.
[27] H. J. S. Sand, *Philos. Mag.* **1901**, *1*, 45.
[28] G. X. Li, Z. Liu, Q. Q. Huang, Y. Gao, M. Regula, D. W. Wang, L. Q. Chen, D. H. Wang, *Nat. Energy* **2018**, *3*, 1076.
[29] H. Ye, S. Xin, Y. X. Yin, J. Y. Li, Y. G. Gu, L. J. Wan, *J. Am. Chem. Soc.* **2017**, *139*, 5916
[30] H. N. He, L. Zeng, D. Luo, J. He, X. L. Li, Z. P. Guo, C. H. Zhang, *Adv. Mater.* **2023**, *35*, 2211498.
[31] P. Xiao, H. B. Li, J. Z. Fu, C. Zeng, Y. H. Zhao, T. Y. Zhai, H. Q. Li, *Energy Environ. Sci.* **2022**, *15*, 1638.
[32] X. Z. Yang, C. Li, Z. T. Sun, S. Yang, Z. X. Shi, R. Huang, B. Z. Liu, S. Li, Y. H. Wu, M. L. Wang, Y. W. Su, S. X. Dou, J. Y. Sun, *Adv. Mater.* **2021**, *33*, 2105951.
[33] Y. H. Zhang, C. K. Chan, *J. Phys. Chem. A* **2002**, *106*, 285.
[34] L. S. Han, Y. M. Guo, F. H. Ning, X. Y. Liu, J. Yi, Q. Luo, B. H. Qu, J. L. Yue, Y. F. Lu, Q. Li, *Adv. Mater.* **2024**, *36*, 2308086.
[35] H. B. Michaelson, *J. Appl. Phys.* **1950**, *21*, 536.
[36] M. S. Zhu, J. P. Hu, Q. Q. Lu, H. Y. Dong, D. D. Karnaushenko, C. Becker, D. Karnaushenko, Y. Li, H. M. Tang, Z. Qu, J. Ge, O. G. Schmidt, *Adv. Mater.* **2021**, *33*, 2007497.
[37] W. H. Ma, S. F. Wang, X. W. Wu, W. W. Liu, F. Yang, S. D. Liu, S. C. Jun, L. Dai, Z. X. He, Q. B. Zhang, *Energy Environ. Sci.* **2024**, *17*, 4819.
[38] F. Shen, H. Du, H. Y. Qin, Z. W. Wei, W. Kuang, N. Hu, W. S. Lv, Z. H. Yi, D. Huang, Z. J. Chen, H. B. He, *Small* **2024**, *20*, 2305119.
[39] W. Zhang, Y. H. Dai, R. W. Chen, Z. M. Xu, J. W. Li, W. Zong, H. X. Li, Z. Li, Z. Y. Zhang, J. X. Zhu, F. Guo, X. Gao, Z. J. Du, J. T. Chen, T. L. Wang, G. J. He, I. P. Parkin, *Angew. Chem.Int. Ed.* **2023**, *62*, 2022126.
[40] H. Pan, Y. Shao, P. Yan, Y. Cheng, K. S. Han, Z. Nie, C. Wang, J. Yang, X. Li, P. Bhattacharya, K. T. Mueller, J. Liu, *Nat. Energy* **2016**, *1*, 16039.
[41] F. H. Cui, D. S. Wang, F. Hu, X. Yu, C. Guan, G. H. Song, F. Xu, K. Zhu, *Energy Storage Mater.* **2022**, *44*, 197.
[42] S. D. Pu, B. K. Hu, Z. X. Li, Y. Yuan, C. Gong, Z. Y. Ning, C. Chau, S. X. Yang, S. M. Zhang, L. Q. Pi, Y. B. T. Tang, J. L. Yue, T. J. Marrow, X. W. Gao, P. G. Bruce, A. W. Robertson, *Joule* **2023**, *7*, 366.